Cycling tests of a reversible BaCe0.8Zr0.1Y0.1O3–δ electrolyte-based protonic ceramic cell with SmBa0.5Sr0.5Co1.5Fe0.5O5+δ oxygen electrode

Paul Pers, Anna Marsicano, Daniel Schmider, Christophe Hartung, Julian Dailly, Gilles Taillades

Cycling tests of a reversible $BaCe_{0.8}Zr_{0.1}Y_{0.1}O_{3-\delta}$ electrolyte-based protonic ceramic cell with $SmBa_{0.5}Sr_{0.5}Co_{1.5}Fe_{0.5}O_{5+\delta}$ oxygen electrode

P. Pers[a], A. Marsicano[a]*, D. Schmider[b], C. Hartung[a], J. Dailly[b], and G. Taillades[a]
[a]Institut Charles Gerhardt Montpellier, Université de Montpellier, 1919 Route de Mende 34293 Montpellier cedex 5, France.
[b]European Institute for Energy Research (EIFER), Emmy-Noether-Str. 11, 76131 Karlsruhe, Germany.
*Corresponding author: anna.marsicano@umontpellier.fr

Abstract
Cells based on proton-conducting ceramics (PCC) working at intermediate temperatures have intrinsic properties that suggest promising potential applications. Currently, almost all the literature in the field of PCC has focused on hydrogen conversion (Protonic Ceramic Fuel Cell PCFC) and/or hydrogen production (Protonic Ceramic Electrolysis Cell PCEC). Very few studies have inspected the reversibility of these systems (RePCC) in order to understand their potential coupling to intermittent renewable energies. Despite the promising results achieved, the development of these technologies remains very challenging.
The work presented here illustrates the fabrication and the characterization of a 32 mm–diameter hydrogen-electrode-supported cell. A double perovskite with general formula $AA'BB'O_{5+\delta}$ is used as air electrode material ($SmBa_{0.5}Sr_{0.5}Co_{1.5}Fe_{0.5}O_{5+\delta}$, SmBSCF) exhibiting very good stability under water vapor- and carbon dioxide-containing atmosphere.
The maximal power density of the Ni-$BaCe_{0.8}$ $Zr_{0.1}Y_{0.1}O_{3-\delta}$ (Ni-BCZY81)/ BCZY81/ SmBSCF cell corresponds to 0.58 W cm^{-2} at 600 °C in fuel cell mode and a current density of j=0.8 A cm^{-2} is measured at 1.3 V and 600 °C in electrolysis mode. The results were collected over a total working time of 280 hours. The cell was stressed with several complete shutdowns and restarting protocols exhibiting an overall remarkable reversibility and durability.

Keywords:
Protonic Ceramic Fuel Cell, Protonic Ceramic Electrolysis Cell, Reversibility, BCZY81, SmBSCF

1 Introduction

Renewable energy sources such as solar and wind produce intermittent electricity therefore several viable storing and delivering options are investigated today. Reversible electrochemical cells can provide an efficient and cost-effective solution for storing electrical energy by splitting water electrochemically in the electrolysis mode and by generating power in fuel cell mode. The variety of reversible electrochemical cells ranges between low- and high-temperature cells, typically proton exchange membrane fuel cells (PEMFCs) and proton exchange membrane electrolyzes (PEMELs) as opposed to solid oxide fuel cells (HT- SOFCs) and solid oxide electrolysis cells (HT-SOECs). Within this framework, the intermediate-temperature reversible proton ceramic cells (RePCCs) can economically produce pure dry hydrogen and high efficiency under various fuels [1–3]. The first noteworthy previous

work on the reversibility of these devices dates from 2017. Specifically, Dailly et al. studied the effect of reversibility (7 cycles) at 600 °C and 700 °C over 2000 hours, showing a very small degradation (2%/kh) [4,5]. In 2019, Choi et al. [6] presented reversibility (12 cycles) at 550 °C over 50 hours. Duan et al. [3] performed a study for 30 cycles totaling around 75 hours with an overall efficiency of 74%. Lately, Ding et al. [7] demonstrated reversible operation between water electrolysis and electricity generation. The electrochemical cell with a $PrNi_{0.5}Co_{0.5}O_{3-\delta}$ oxygen electrode and $BaCe_{0.4}Zr_{0.4}Y_{0.1}Yb_{0.1}O_{3-\delta}$ electrolyte was run at various voltages alternating between the PCEC and PCFC working modes for 600 hours at 500 °C.

Despite these recent developments, the real performances of RePCCs do not meet the expected ones, due to a large extent to the activity towards water oxidation/oxygen reduction reactions of the air electrode. Thus, it is crucial to develop air electrode materials that maintain high electrocatalytic activity enabling fast oxygen reduction kinetics and low over-potentials at the intermediate working temperatures. Layered perovskite oxides with the general formula $AA'B_2O_{5+\delta}$ have drawn the attention of various research groups [8–12] because their chemical diffusion and surface exchange coefficients are significantly higher than those of ABO_3-type perovskite oxides,.

Fuel cells that associate a proton-conducting ceramic electrolyte and $AA'B2O_{5+\delta}$ cathode materials have been the subject of a great amount of work. For example, at 700 °C a cell with a $GdBaCo_2O_{5+\delta}$ cathode printed on a $BaCe_{0.7}Zr_{0.1}Y_{0.2}O_{3-\delta}$ (BCZY712) electrolyte attained a power density of 0.266 W cm^{-2} [13]. Higher performances of 0.382 and 0.533 W cm^{-2} at 700 °C using $SmBaCo_2O_{5+\delta}$ and $SmBa_{0.5}Sr_{0.5}Co_2O_{5+\delta}$, respectively, were obtained by the same authors [14,15].

A single cell with a $BaCe_{0.7}Zr_{0.1}Y_{0.1}Yb_{0.1}O_{3-\delta}$ electrolyte and the layered double-perovskite cathode $NdBa_{0.5}Sr_{0.5}Co_{1.5}Fe_{0.50}O_{5+\delta}$ (NdBSCF) achieved a maximum power density (MPD) of 1.61 W cm^{-2} at 750 °C [16]. $PrBa_{0.5}Sr_{0.5}Co_{1.5}Fe_{0.5}O_{5+\delta}$ (PrBSCF), was reported to deliver a power density of 0.5 W cm^{-2} at 500 °C associated with $BaZr_{0.4}Ce_{0.4}Y_{0.1}Yb_{0.1}O_{3-\delta}$ [17].

To the best of our knowledge, the Samarium-containing analogue $SmBa_{0.5}Sr_{0.5}Co_{1.5}Fe_{0.5}O_{5+\delta}$ (SmBSCF) has not been reported as air electrode for PCC to date, whereas, according to Jun et al. [18] SmBSCF

demonstrates better redox stability and electrochemical performance under typical fuel cell operating conditions and combines fast oxygen diffusion with high surface kinetics. In association with $Ce_{0.9}Gd_{0.1}O_{2-\delta}$ (GDC), it exhibits low area-specific resistance (ASR) values of 0.081 Ω cm^2 and excellent cell performances. SmBSCF is indeed a promising material as a cathode for IT-SOFC systems.

In this work, the SmBSCF air electrode synthesized by the Glycine Nitrate Process was associated to $BaCe_{0.8}Zr_{0.1}Y_{0.1}O_{3-\delta}$ (BCZY81): the electrochemical performances of a single cell was evaluated under diverse operation conditions including fuel cell/electrolysis, thermal and shutdown/restart cycling.

2 Experimental

2.1 Material synthesis and characterizations

The electrolyte nano-powder $BaCe_{0.8}Zr_{0.1}Y_{0.1}O_{3-\delta}$ (BCZY81) was obtained using metal nitrates $Ba(NO_3)_2$, $ZrO(NO_3)_2{\cdot}6H_2O$, $Ce(NO_3)_3{\cdot}6H_2O$ and $Y(NO_3)_3{\cdot}6H_2O$ (Aldrich, 99.9%) as starting materials for the Glycine-Nitrate combustion Process (GNP). Ethylene diamine tetra-acetic acid (EDTA) was not added at any step of the synthesis. The appropriate molar ratio of metal nitrates was dissolved in deionized water under heating the beaker on a heating plate. Glycine was then added to the nitrate solution. The molar ratio of glycine to the total metal cations was set to 1.5:1. Then, the proper volume of ammonia solution was slowly dropped into this mixture until a clear solution was obtained (pH 6-7). On evaporation of water, a yellow gel was gradually formed. At this point the beaker was placed in an oven pre-heated at 600 °C in air and at ambient pressure. The combustion reaction took place within a few minutes, forming the as-synthesized powders. Subsequently, the powder was cooled, manually mixed and finally calcined at 900 °C with a 3 h ramp for 4 h in ambient conditions to obtain the final desired BCZY81 composition. SmBSCF was synthetized following the same GNP combustion preparation method as that used for the electrolyte powder with $Sm(NO_3)_3{\cdot}6H_2O$, $Ba(NO_3)_2$, $Sr(NO_3)_2$, $Co(NO_3)_2{\cdot}6H_2O$ and $Fe(NO_3)_3{\cdot}9H_2O$ (99.99% purity, Sigma-Aldrich) metal nitrates as precursors. The air electrode powder was also calcined at 900 °C in air.

The synthesized powders were studied by X-ray diffraction using a PANalytical X'Pert diffractometer with $CuK_{\alpha 1,2}$ radiation equipped with an X'Celerator detector. XRD patterns were recorded over an angular range of 2θ = 20-90° with a step size of 0.016°. The microstructure of the single cell was characterized by scanning electron microscopy (SEM, FEI Quanta 200).

2.2 Cell manufacturing

The BCZY81-based cell with SmBSCF as oxygen electrode was manufactured using industrial fabrication routes associating tape casting for the substrate and spraying techniques for the electrolyte and air electrode depositions.

The hydrogen electrode slurry was prepared by mixing powders $BaCe_{0.8}$ $Zr_{0.1}$ $Y_{0.1}$ $O_{3-\delta}$ (BCZY81, Cerpotech) /NiO (J.T.Baker®) 40:60 wt% , solvents (Ethanol/methyl ethyl ketone) and a dispersing agent in a TURBULA® type T2F (WAB). After 22 h of mixing, polyvinyl butyral binder and two plasticizers were added separately, with further mixing for 1 h after the first two steps and 3 h after the last addition. After a 1-day standing period, air was removed from the slurry under low vacuum. The slurry was then cast on a silicon-coated PET film using a ZAA 2300 automatic film applicator coater (Zehntner GmbH, Switzerland), and then dried for 12 h at room temperature, in a confined box under ventilation to help remove solvent vapors [4].

The electrolyte was deposited by Wet Powder Spraying (WPS), as described in previous works [19]. For this purpose, the BCZY81 and LiZnO sintering aid (3 molar %) powders were dispersed (3 wt.% of BCZY81) into isopropanol (99.5% purity, Sigma-Aldrich) under ultrasonic irradiation to form a stable suspension. No further additives were used, such as binders, plasticizers, or dispersants. The suspension was sprayed onto a fresh substrate cut in a round shape (ø 40 mm), using a Spray Coater ND-SP from Nadetech Innovations®. Air was used as the carrier gas at a working pressure of 1.3 atm. The spray process was carried out at a substrate temperature of 55 °C with the help of a hot plate. 13 40-mm square layers were sprayed with a suspension flow rate of 50 ml h^{-1} with a nozzle velocity of 700 mm min^{-1} resulting in a deposition of 0.8 ml cm^{-2}. The half-cell was then sintered in air at 1350 °C

for 6 h using a ramp of 1 °C/min, attaining a final diameter of 32 mm with a final fuel electrode and electrolyte thicknesses of approximately around 500 µm and 5 µm.

The oxygen electrode suspension was prepared following the same protocol as that for the electrolyte. A mask was placed and centered on the sintered half-cell to obtain a round-shaped electrode deposition (ø 12 mm) of 55 WPS layers (0.8 wt.% of SmBSCF in isopropanol) with 3.02 ml cm^{-2}. The final assembly was calcined at 1050 °C for 1.5 h in air using 5 h heating and cooling ramps, leaving an air electrode layer of 15 µm with an average agglomerate size of 420 nm (Figure S 7).

2.3 Cell testing conditions

The single cell was tested in a Fiaxell® Open Flange fuel cell test bench in the 500 to 700 °C temperature range. The current collection was performed using gold wires connected to a gold mesh (ø 16 mm) on the air side and nickel wires connected to a nickel mesh set on a stainless-steel support on the fuel side. Electrochemical measurements (IV and IP curves) were carried out using a potentiostat/galvanostat (Biologic® SP150). Electrochemical impedance Spectroscopy measurements were performed over the frequency range from 0.1 Hz to 1 MHz with an AC voltage amplitude of 10 mV.

The performance and durability of the cell were examined following a test protocol that included an activation step, three complete shutdowns and six fuel cell / electrolysis cycles. Figure 1 depicts the current profile applied to the cell during the 4 weeks test.

The primary fundamental step consisted in the activation of the cell. This involved an initial heating to 700 °C with the hydrogen electrode under 5% of H_2 in Argon ($Ar/5H_2$) and the air electrode under air. Once the setpoint temperature was reached, the hydrogen electrode was fed with a hydrogen flux of 150 ml min^{-1} until the open circuit voltage (OCV) reached 1.04 V. Afterwards, IV curves were acquired at different temperatures between 700 °C and 550 °C before and after the activation protocol, which consisted in stabilizing the cell at 600 °C, at around 0.7 V under a constant current of 0.35 A cm^{-2}. Finally, the working temperature was kept at 600 °C throughout the entire test.

Then, the cell was stressed with a series of complete shutdowns to room temperature followed by quick reactivation protocols up to 600 °C. Throughout all the test, the reversibility experiments were performed between -0.35 A cm^{-2} (electrolysis mode) and 0.35 A cm^{-2} (fuel cell mode). 150 ml min^{-1} of non-humidified H_2 and 300 ml min^{-1} of non-humidified air were the fluxes chosen in fuel cell mode. During electrolysis steps, purified water was added on the air side using a peristatic pump, the experiments were carried out at 1.2 V at the operating conditions consisting in 66 ml min^{-1} of H_2 flux at the fuel electrode and 166 ml min^{-1} of synthetic air and an equivalent 60 ml min^{-1} of gas water flux at the air electrode.

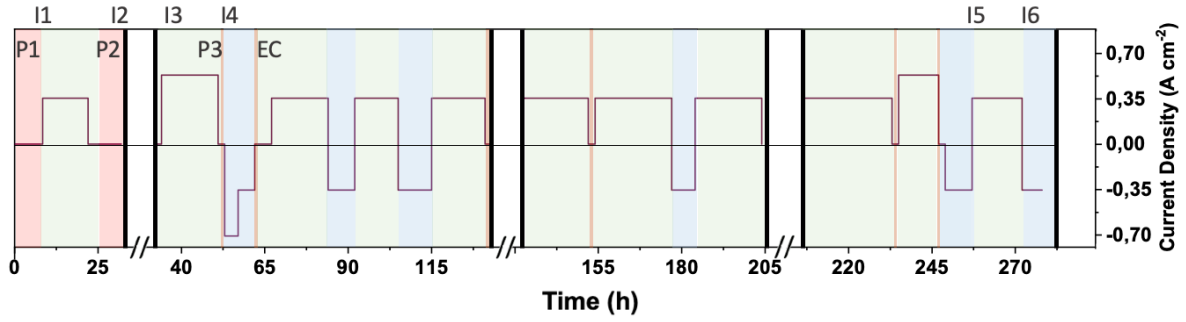

Figure 1: The current profile used during the long-term test. The abscissa values indicate the effective absolute operation time. On the profile, P1 to P3 and EC legends indicate when polarization curves were acquired in FC and EC mode respectively. On the top I1 to I6 legends highlight when impedance spectra were acquired. Temperature-dependent IV curve acquisitions are highlighted in red. Fuel cell and electrolysis periods at 600 °C are indicated with green and blue backgrounds, respectively.

3 Results and discussion

3.1 Structure and morphology

The XRD diffraction patterns of the sintered BCZY81 and SmBSCF powders are presented in Figure 2a and 2b respectively.

BCZY81 powder sintered at 900 °C shows an orthorhombic symmetry with the space group Imma (74) (reference structure $BaCe_{0.8}Y_{0.2}O_{2.9}$ with ICSD code 193458). The lattice parameters and the cell volume of BCZY81 coincide with those reported in the literature [9,18,20]. The XRD data were also acquired on the half-cell after sintering at 1350 °C for 6, revealing lattice constants of a = 6.2015(1) Å, b = 8.7247(3) Å, c = 6.2204(1) Å (Figure 2) by a Le Bail refinement (R_p=2.16%, R_{wp}=3.76%).

The SmBSCF specimen calcined for 1.5 hours at 1050°C is also well crystallized. No secondary phase is detected (Figure 2b), and the XRD peaks are consonant with the double perovskite structure of $SmBaFe_2O_{5.439}$ reference (ICSD 48770). Le Bail profile data refinement reveals that the diffraction patterns of SmBSCF can be indexed to a tetragonal structure (space group P4/mmm) with unit-cell parameters a = b = 3.851(1) (9) Å, c = 7.6220(3) Å (R_p=1.89%, R_{wp}=2.67%). Averaging the results obtained from the 5 most intense peaks of the diffractograms the coherent diffraction domain sizes were obtained using the Debye-Scherrer equation for the two compositions before and after sintering (Table S 1). An in-depth morphological characterization of the calcinated BCZY81 and SmBSCF powders was performed by TEM. A fine grain size distribution between 35 and 58 nm was found for BCZY81 and a larger distribution between 18-80 nm was found for SmBSCF (Figure S 3). The composition results obtained by EDX are close to those expected for BCZY81 and SmBSCF (Figure S 5). A different outcome is expected on the powders due to the irregular surface of characterized. Ultimately, this is confirmed by the analysis of the dense, flat and compact electrolyte on the half cell (Figure S 5).

Additionally, the stability of SmBSCF is tested over 5 hours under pure CO_2 and over 16 hours under pure H_2O at 600 °C (Figure 2d-e). SmBSCF is confirmed to be stable under both electrochemical testing relevant atmospheres.

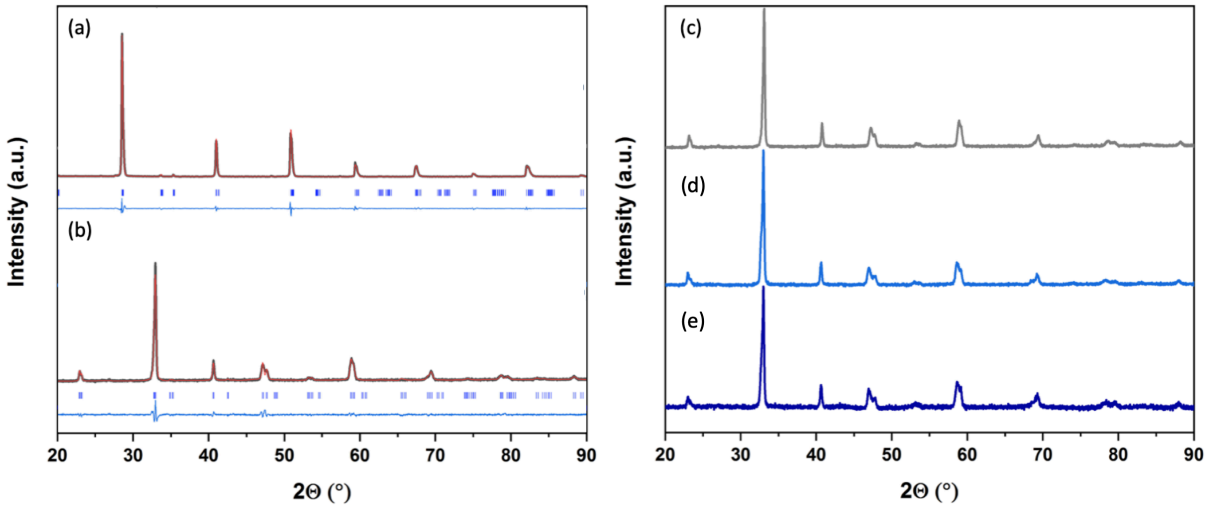

Figure 2: Le Bail refined XRD patterns for (a) BCZY81 layer on the half-cell sintered at 1350 °C for 6 h, (b) and (c) SmBSCF powder calcinated at 1050 °C for 1.5 h, XRD patterns of SmBSCF powder treated under CO_2 (d) and H_2O (e) atmospheres at 600 °C or 5 h and 16 h respectively.

3.2 Electrochemical characterization

The test profile, presented in Figure 1, was chosen in order to examine the impact of the initial activation protocol, the reversibility of the cell performances in fuel cell and in electrolysis conditions, and the durability of the cell after complete shutdowns and restarts. Figure 3 shows the evolution of the potential of the button cell of 32 mm in diameter with an active area of 1.13 cm^2 (corresponding to the area of the SmBSCF oxygen electrode) during the whole test (280 h). The results will be discussed on the basis of the polarization curves (P1 to P3 and EC) and on the interpretation of the impedance diagrams denoted I1 to I6 on Figure 3.

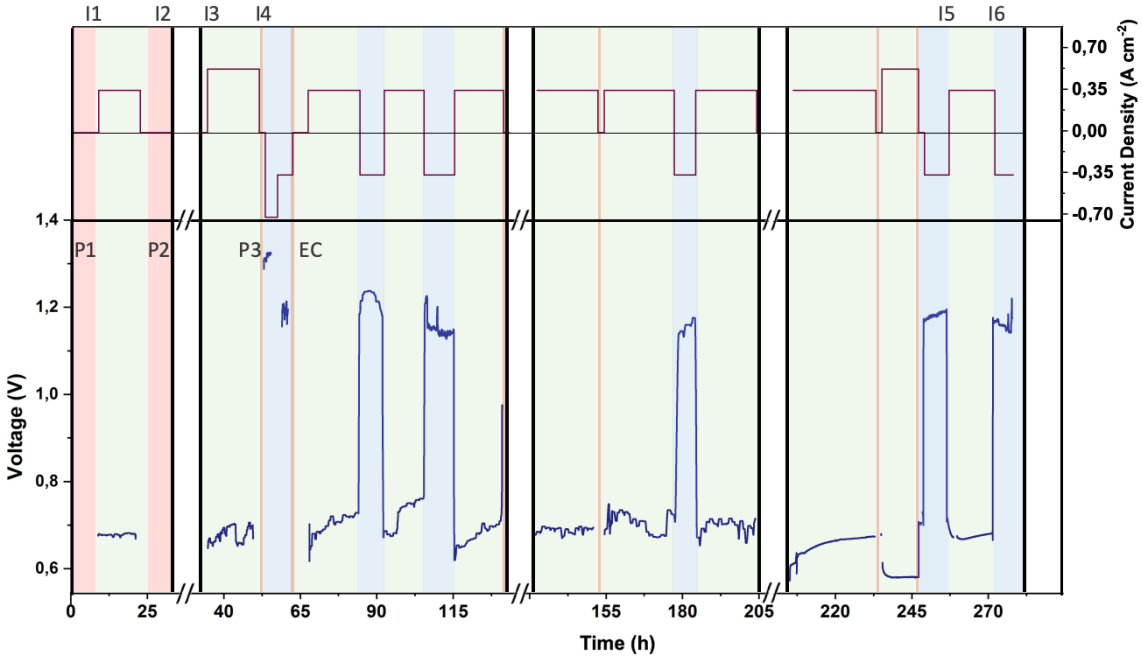

Figure 3: Evolution of the cell potential and current during the whole test. Red backgrounds indicate temperature-dependent IV curves acquisitions (P1 and P2). Orange vertical lines highlight when polarization curves at 600°C were acquired (P3 and EC). The green and the blue background highlight the fuel cell and electrolysis period during cycling, respectively. The white areas indicate when a full shutdown was performed. I1 to I6 are linked to EIS acquisitions.

Activation

Once the temperature of 700 °C is reached, the gas supply at the fuel side is switched to pure hydrogen in order to complete the reduction of the nickel oxide. Then, the activation is accomplished by maintaining the temperature at 600 °C and fixing the potential of the cell at 0.7 V under galvanostatic

conditions for 12 hours. Figure 4 (a) and (b) compare the performances at various temperatures of the cell before and after the activation step.

In both cases, Open Circuit Voltages (OCV) above 1.1 V are measured at 600 °C, suggesting a gas-tight, highly-dense and pure ionic-conducting electrolyte in the operating conditions.

The first fuel cell performance (P1) is already very promising with a maximum power density (MPD) of 0.4 W cm^{-2}; this MPD increases remarkably after the cell activation reaching 0.58 W cm^{-2} at 600 °C.

Indeed, it is well known that the electrode performances improve significantly after the application of a cathodic polarization [21]. Clearly, the activation process is a very important phenomenon, and it is of great practical relevance because the electrode performance not only depends on the fabrication process - i.e., the microstructure, but also on the testing history. Unfortunately, little is known on the mechanism of the activation process under cathodic polarization, and the activation phenomena are poorly documented in the case of protonic ceramic cells.

From the electrochemical impedance spectroscopy spectra (EIS) collected at different temperature the Arrhenius plot could be reconstructed and the activation energies are derived. It is clear that after the activation the ohmic component is exclusively linked to a pure proton conduction with an activation energy of 0.4 eV (Figure 4c).

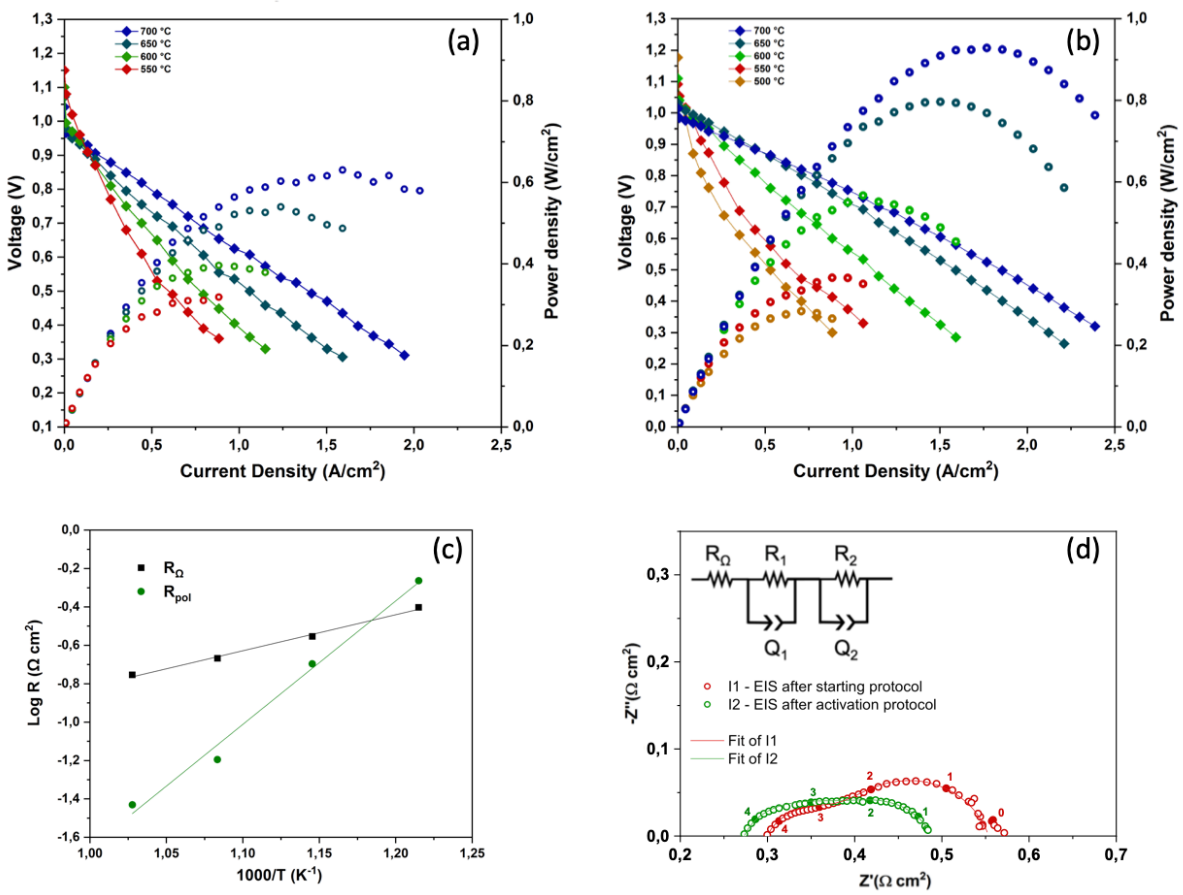

Figure 4: Temperature dependent polarization and power density curves of the cell before (a)- i. e. at P1- and after (b) - i. e. at P2 - the application of the activation protocol. (c) Ohmic and polarization resistance of the single cell at different temperatures under open circuit conditions. (d) The EIS responses measured at open circuit at 600 °C before (I1 - red) and after (I2 - green) the activation. On the top, the schematic representation of the equivalent circuit used to model the EIS experimental spectra.

Figure 4d shows the Nyquist plots of the EIS measurements performed before (I1) and after (I2) the activation step at 600 °C. The ohmic resistance of the single cell (R_Ω) is found at the high-frequency intercept. R_Ω includes the resistive contributions of the electrolyte, the two electrodes, the current collectors and the wires. The R_Ω of the current collectors and of the wires can be ignored since it measures less than 0.01 Ω. The total resistance (R_Ω + R_P) of the cell is found at the low frequency intercept of the EIS spectra. R_{tot} contains the ohmic resistance of the cell, the concentration polarization resistance given by mass transfer or gas-diffusion polarization, and the charge transfer resistances related to the electrochemical reactions at the electrode surface.

The two EIS spectra acquired before and after the activation step (Figure 4d) are fitted using an equivalent circuit model consisting of a resistive element and two RQ elements (a resistance R and a

constant phase element Q in parallel). The EIS data after the activation (I2) are accurately fitted using this equivalent circuit, resulting in a total error of less than 1%, while in the case of I1, a difficult to quantify third contribution appears at low frequencies (Table 1). Generally, the LF (10^{-1} - 1 Hz) contribution is considered to relate to gas adsorption/desorption and gas diffusion in the porous framework of the electrodes. Hydrogen diffuses significantly faster in the fuel electrode cermet compared to water or oxygen molecules within the oxygen electrode. Therefore, it is reasonable to link this LF contribution to mass transfer processes at the oxygen electrode.

The orders of magnitude relative to the high frequency (HF) arc parameters (f_{HF}= [1 kHz - 10 kHz], C_{HF} = 10^{-3} F cm^{-2}) and to the medium frequency (MF) arc parameters (f_{HF}= [1 Hz - 100 Hz], C_{HF} = 10^{-2} F cm^{-2}) allow us to identify two contributions. Thus, according to the literature [22], the HF arc is related to the charge-transfer processes at the electrode/electrolyte interface and the MF arc is correlated to dissociative absorption, the transfer of species at the TPB and surface diffusion [23,24]**.** Even if we could not completely exclude at this stage charge transfer and surface reactions at the H_2 electrode, considering a previous study on H_2 electrodes [25], these two contributions can be, as a first approximation, ascribed exclusively to the oxygen electrode.

Moreover, this hypothesis is reinforced by the activation energy value obtained for the total polarization resistance (1.28 eV), which is equivalent to what found for the same oxygen electrode material [26] in Figure 4c.

	Temperature (°C)	R_o (Ω cm^2)	f_o (Hz)	R_1 (Ω cm^2)	f_1 (Hz)	C_1 (F cm^{-2})	R_2 (Ω cm^2)	f_2 (Hz)	C_2 (F cm^{-2})	R_1+R_2 (Ω cm^2)
Before Activation	700	0.20	9354	0.02	1066	0.0084	0.06	49	0.0667	0.08
	650	0.24	18847	0.04	2835	0.0020	0.13	44	0.0339	0.17
	600 (I1)	0.30	23808	0.07	1706	0.0013	0.18	30	0.0373	0.25
	550	0.40	47988	0.15	2936	0.0004	0.41	20	0.0260	0.56
	Activation Energy	0.32 eV		0.88 eV			0.84 eV			0.84 eV
After Activation	700	0.18	7540	0.02	1467	0.0110	0.02	57	0.1695	0.04
	650	0.21	11816	0.03	2235	0.0031	0.03	75	0.0791	0.06
	600 (I2)	0.28	23808	0.09	2269	0.0010	0.10	43	0.0226	0.19
	550	0.40	37998	0.17	4103	0.0003	0.33	50	0.0057	0.50
	Activation Energy	0.37 eV		1.11 eV			1.37 eV			1.28 eV

Table 1: Fitting parameter values obtained from EIS spectra before and after the activation protocol. The R1+ R2 values correspond to the total polarization ASR (R_{pol}).

The comparison of the two EIS spectra (I1 and I2, Table 1) reveals a decrease in the ohmic contribution from 0.30 to 0.28 Ω cm^2 and a decrease in the MF polarization contribution from 0.18 to 0.1 Ω cm^2, indicating an increase in the electrochemical activity of the oxygen electrode. The conventional explanation for the activation process on oxygen electrodes is based on the formation of oxygen vacancies at the electrode/electrolyte interface region under polarization [27]. Microstructural changes under polarization can also be considered and these have been reported, for example, on LSM-based electrodes by various research groups. Jiang et al. [21] reported the disappearance of large agglomerates and the consequent formation of much smaller and well-defined granular-shaped particles with clear boundaries after various polarization treatments.

Shutdown/restart switching effects

The working conditions of a fuel cell are guaranteed by the electrocatalytic activity, the ionic- and-electronic conduction of the electrodes and the proton diffusion capability of the electrolyte. Nevertheless, the durability of the cell is a fundamental aspect to consider. A fuel cell should demonstrate an excellent resistance to temperature changes and thermal shocks and an ability to restart quickly after emergency or routine/maintenance shut-downs [28,29].

To this end, a shutdown cycling protocol is applied. The cell is interrupted at the operating temperature by stopping the pure H_2 supply and turning off the furnace allowing the cell to cool to room temperature with an Ar/5%H_2 feed at the fuel electrode and maintaining the air feed at the air electrode. A brief restarting time of 2 hours is used after the three shutdowns to reach the operating temperature.

The OCV is monitored during the heating ramps applied after each shutdown (Figure 5a). The OCV increases to a pseudo-plateau around 0.85 V under Ar/5%H2 and reaches values under 1V after switching to pure H_2. The profiles are similar for all restarts. The plot in Figure 5b evidences that the activation process under current allows to restore a high OCV close to the initial one.

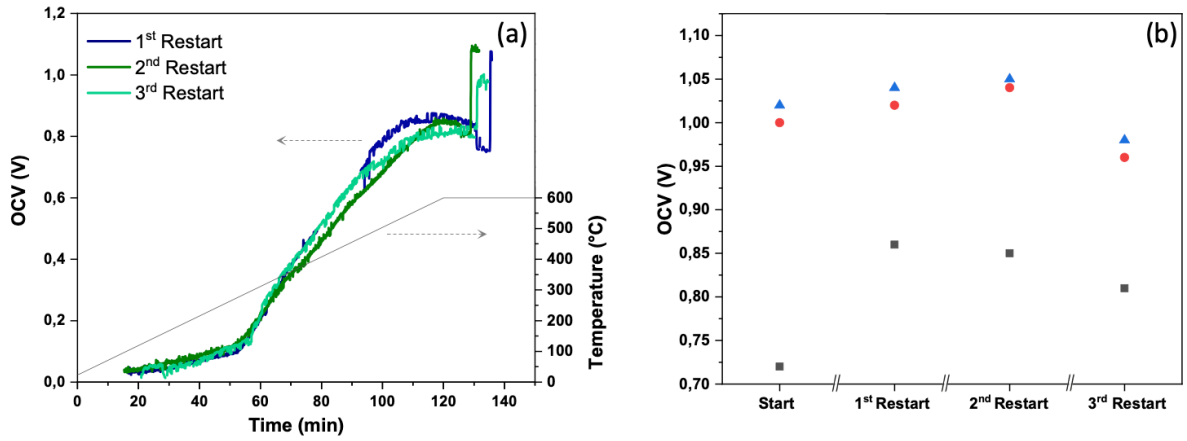

Figure 5 : Open Circuit Voltage (OCV) as a function of tempéraure during the restart procedures (a) and OCV at 600°C measured at diferent stages of the restart procedure (■: after the temperature ramp under Ar/5%H_2, ●: under pure H_2 and ▲: after 10 h under constant current (b).

The cell is then maintained under current at 0.7 V for 10 hours under pure H_2. The effects of the thermal cycling and the interruption of the fuel supply are quantified by EIS measurements. The comparison between the impedance spectra before and after the first shutdown (Figure 6, Table 2) shows an irreversible loss of the ohmic resistance from 0.27 (I2) to 0.34 Ω cm^2 (I3). This feature suggests changes in the properties, microstructure and/or catalytic activity of the negative electrode. During the cooling and heating periods, the fuel electrode of the cell is fed with diluted H_2, so that Ni is not easily oxidized. However, thermal cycling causing thermal expansion mismatch might alter the network of electrolyte grains, which normally prevent Ni agglomeration in the fuel electrode, resulting in Ni clusters disrupting electronic conduction routes, and increasing ohmic resistances [30]. As shown in Figure 6, the polarization area specific resistance (ASR) increases drastically after the restart of the cell (from 0.21 to 0.51 Ω cm^2) and decreases to 0.27 Ω cm^2 after the activation under constant current (I4). The analysis of the impedance spectra by the equivalent circuit model (in Figure 4d) allows to separate the HF (R1) and MF (R2) contributions. Comparing I2, I3 and I4 (Table 2), both R1 and R2 fitted values show an almost-fully-reversible contribution mainly related to the air electrode reactions. However, the non-reversible part of the HF arc reveals a disrupted charge-transfers at the fuel electrode, whereas the charge-transfer at the oxygen electrode seems reversible throughout the shutdown/restart processes. Unfortunately, nothing is known about the de-activation/activation

process of the SmBSCF electrode contributing in the MF range and the activation phenomena of the air electrode are poorly documented. A possible explanation of this behavior, already proposed for $(Ba,Sr)_1(Co,Fe)_1O_{3-\delta}$ [31] or $(La,Sr)_1(Co,Fe)_1O_{3-\delta}$ perovskites [32], is the increase of oxygen vacancy concentration under polarization with a consequent gain in the oxygen reduction activity of the electrode.

Clearly, the reactivation process after a shutdown/restart cycle is a very important phenomenon and is of great practical relevance for the electrode performances. Consequently, with the increase of the total ASR of the cell, the performances of the cell lower with a MPD going from 0.580 W cm^{-2} (P2) to 0.470 W cm^{-2} (P3).

	Values from the equivalent circuit model								Experimental ASR		
EIS Spectra 600 °C	R_o (Ω cm^2)	R_1 (Ω cm^2)	f1 (Hz)	C_1 (F cm^{-2})	R_2 (Ω cm^2)	f2 (Hz)	C_2 (F cm^{-2})	R1+R2 (Ω cm^2)	ASR_W (Ω cm^2)	ASR_{pol} (Ω cm^2)	ASR_{tot} (Ω cm^2)
I1	0.30	0.07	1706	0.0013	0.18	30	0.0373	0.25	0.30	0.27	0.57
I2	0.27	0.09	2269	0.0010	0.10	43	0.0226	0.19	0.27	0.21	0.48
I3	0.34	0.28	1100	0.0005	0.23	108	0.0063	0.51	0.34	0.51	0.85
I4	0.33	0.11	1743	0.0009	0.16	140	0.0041	0.27	0.33	0.27	0.60
I5	0.35	0.22	1412	0.0005	0.17	79	0.0124	0.39	0.35	0.39	0.74
I6	0.36	0.18	2178	0.0004	0.09	100	0.0170	0.27	0.36	0.27	0.63

Table 2: Area specific resistances, capacitances and frequencies of the arcs resulted from the electric circuit model and the experimental values obtained from the EIS spectra acquired during the whole test.

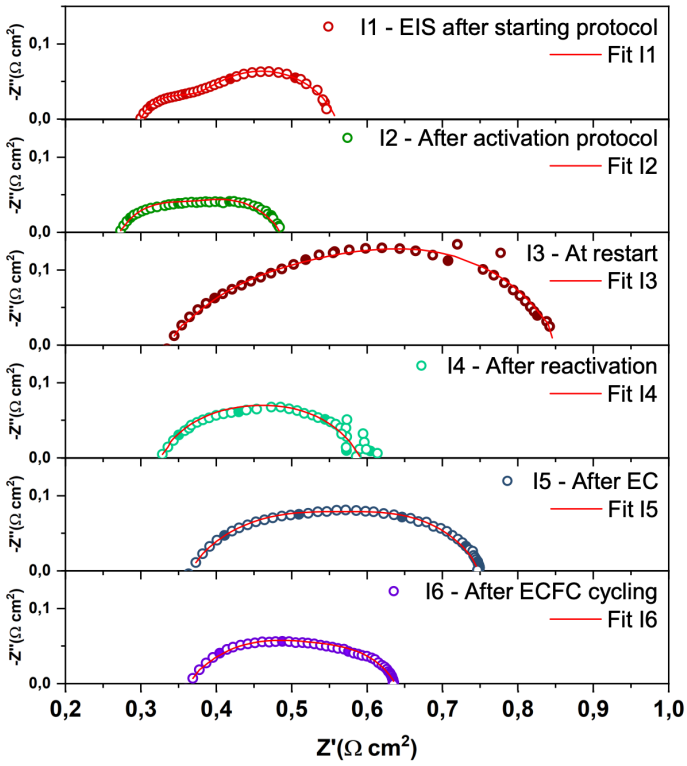

Figure 6: EIS at the OCV at 600 °C collected during the whole test.

Fuel cell / Electrolysis cycling

Compared to other reversible electrochemical cells such as high-temperature solid oxide cells (HT-revSOCs), the steam is supplied or produced at the oxygen electrode side of the protonic ceramic cells, and only dry pure hydrogen is generated or consumed at the hydrogen electrode. This means that the stability requirement of the fuel electrode material is easier and the reversibility is potentially better.

After the first restart and the reactivation under current, the first fuel cell/electrolysis cycle is performed in the 0.3 - 1.5 V potential range in order to have an insight into electrolysis performances and cell reversibility. The polarization behavior obtained is shown in Figure 7 for both electrolysis and fuel cell modes at 600 °C (P3, EC on Figure 3).

The current density at 600 °C and 1.3 V is 0.8 A cm^{-2}, exceeding the results reported on cells with identical electrolytes [4,30,31,33]. This indicates that the SmBSCF oxygen electrode is a performing air electrode for RePCCs. Then, six EC/FC cycles are performed. The change in mode is made by inverting the current density (+/- 0.35 A cm^{-2}) to stabilize the cell potential at around 0.7 V in fuel cell mode and

at 1.2 V in the electrolysis mode. The Figure 5 compares the impedances at OCV after the electrolysis period (I5) and after the 2 EC/FC cycles (I6).

Clearly, the ohmic resistance remains constant during the FC/EC cycling while the polarization resistance increases and an additional contribution at low frequencies appears after the electrolysis experiment (I5 Figure 6 and Table 2). However, the galvanostatic fuel cell periods act as a "recovery mode" that tends to compensate for the degradation. This behavior highlights a reversible phenomenon occurring under electrolysis conditions at the air electrode. One hypothesis consists in a slow evacuation of the excess of water at the air electrode side during electrolysis, the switch to fuel cell mode allows the evacuation of overflowed moisture.

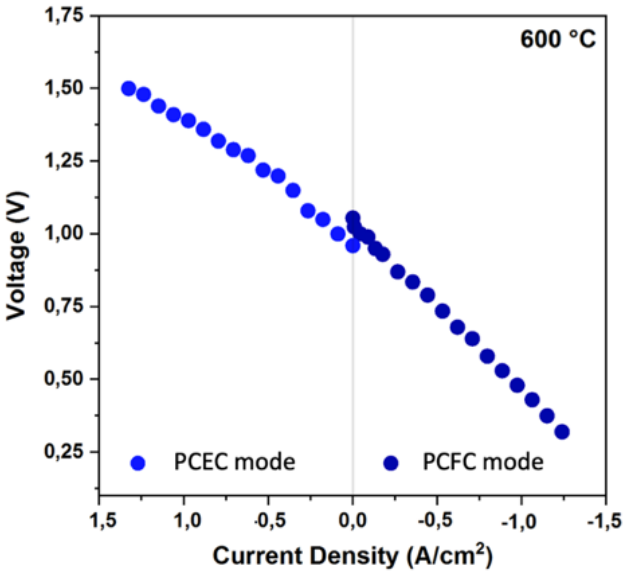

Figure 7: IV curve during the FC/EC cycle (P3, EC). The loss in OCV is linked to change of the gas feed in between the two modes.

3.3 Post-mortem analysis

The post-mortem analysis were performed using SEM and EDX techniques. Figure 8 presents the SEM micrographs of the cell Ni-BCZY81/BCZY81-LiZnO/SmBSCF. The cross-section exhibits the thickness of the fuel electrode, electrolyte and air electrode layers corresponding to 500 µm, 5 µm and 15 µm, respectively. Figure 8 reveals a homogeneous distribution of BCZY81 and Ni phases in the fuel electrode with particle size around 1-2 µm, providing sufficient current collection and porosity for gas diffusion. The electrolyte is dense despite some closed pores observed though its thickness. However,

the separation of fuel and air is sufficient for obtaining a high OCV of 1.1 V at 600 °C. The average size of SmBSCF aggregates remains constant at around 400 nm before and after testing. A coarsening of the agglomerate average size of around 700 nm is detected on the surface layer of the oxygen electrode in contact with the gold grid (Figure S 7). The increase in agglomerate size is probably not due to activation potentials or cell degradation, as most of the reaction sites are not on at the surface. It seems plausible that the "noisy" potential signal shown in Figure 3 indicates a non-optimal contact with the gold grid affecting the microstructure. The distribution of elements on the cross-section and the air electrode surface of the cells is examined by energy dispersive X-ray spectroscopy (EDS). In Figure 8e, the uniform distribution of the different phases and elements is revealed, no diffusion between the different layers is observed.

As shown in Figure 8d, chromium deposition and a slightly higher concentration of Ba are found on the surface of the oxygen electrode. This Cr contamination is caused by the steel gas hose used as water inlet during electrolysis. It has been already reported [34] that the Ba oxide and the Co oxide segregate on the surface of the double perovskite oxide at high temperatures. The Cr reacts easily with Ba, oxide forming $BaCrO_4$ or $BaCr_2O_4$ (Figure S 6) which can cause the deterioration of the performances [35]. To our knowledge, the formation of barium chromate at the oxygen electrode of PCC has not been yet reported. Nevertheless, it is possible to protect the steel surface and limit the Cr reaction occurring at around 550 °C using Cu-Mn or Co-Mn spinels [36].

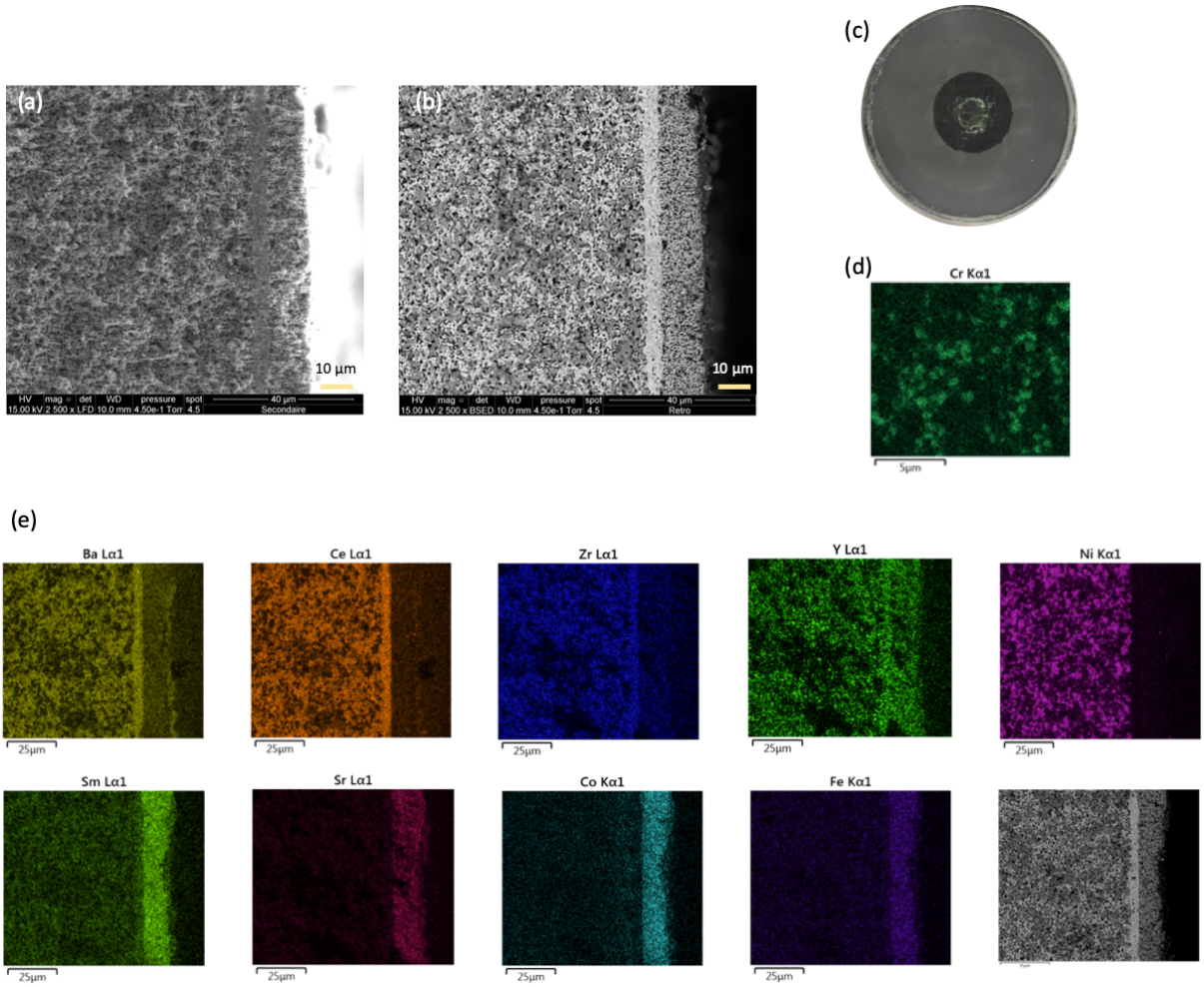

Figure 8: Post-mortem SEM micrographs of the Ni-BCZY/BCZY-LiZnO/SmBSCF cell sintered at 1350°C in secondary electrons (a) and backscattered electrons (b) imaging modes. (c) Picture of the cell after the test. (d) SEM image of the surface of the oxygen electrode with Cr EDX mapping. (e) Cross section SEM image and EDX mapping of Ba, Zr, Sm, Sr, Ni, Ce, Y, Co and Fe elements.

4 CONCLUSION

In this work, a stress test was presented in order to investigate the durability and the performance of a Proton Ceramic Cell. The cell fabricated on a NiO-$BaCe_{0.8}Zr_{0.1}Y_{0.1}O_{3-\delta}$ fuel electrode support with a $BaCe_{0.8}Zr_{0.1}Y_{0.1}O_{3-\delta}$ electrolyte and a $SmBa_{0.5}Sr_{0.5}Co_{1.5}Fe_{0.5}O_{5+\delta}$ oxygen electrode exhibited remarkable performances both in fuel cell and in steam electrolysis modes with a maximum power density of 0.58 W cm^{-2} at 600 °C and a current density at 600 °C under 1.3 V of 0.8 A cm^{-2}, respectively. The excellent performances of the studied cell are attributed to the high activity of the SmBSCF air electrode towards the oxygen evolution and reduction reactions. Moreover, SmBSCF has been shown to be a suitable

electrode material highly compatible with proton-conducting electrolytes. This study is the first to inspect the complete start and stop of PCC and highlights the importance of the activation protocol for increasing the performances and for regenerating the cell after each restart. One possible explanation could be attributed to the capability of the double-perovskite to create oxygen vacancies during the activation period, leading to an increased bulk oxygen diffusion and increased oxygen reduction activity. Throughout the entire working period (3 complete starts and stops and 6 fuel cell / electrolysis cycles), the cell OCV was relatively stable but an irreversible increase of the ohmic resistance due to supposed changes in the hydrogen electrode microstructure is observed at every restart. During cycling between the fuel cell/steam electrolysis mode, the ohmic resistance remained stable and the polarization contribution was completely restored under galvanostatic fuel cell periods. Further investigations have to be performed in order to attain a global understanding of the degradation/stress caused by the complete start and stop and fuel cell/steam electrolysis cycling.

CRediT authorship contribution statement

Paul Pers: Conceptualization, Lead researcher, Methodology, Formal analysis, Investigation. Anna Marsicano: Investigation, Writing and editing manuscript. Daniel Schmider: Cell fabrication, Microstructural analysis, Methodology. Christophe Hartung: Cell test and platform development, Investigation. Julian Dailly: Writing – review and editing original draft, Methodology, Validation. Gilles Taillades: Supervision, Visualization, Writing – review & editing final draft, Funding acquisition.

Declaration of interest

The authors declare that they have no known competing financial interests or personal relationships that could have appeared to influence the work reported in this paper.

Acknowledgements

The authors acknowledge the “Plateforme d’Analyse et de Caracterisation” of the ICG Montpellier. A.M. Acknowledges the financial support from the French National Research Agency through the PEPR project PROTEC - Grant Number ANR-22-PEHY-0006.

References

[1] D. Medvedev, Trends in research and development of protonic ceramic electrolysis cells, Int. J. Hydrogen Energy. 44 (2019) 26711–26740. https://doi.org/10.1016/j.ijhydene.2019.08.130.

[2] L. Bi, S. Boulfrad, E. Traversa, Steam electrolysis by solid oxide electrolysis cells (SOECs) with proton-conducting oxides, Chem. Soc. Rev. 43 (2014) 8255–8270. https://doi.org/10.1039/c4cs00194j.

[3] C. Duan, R. Kee, H. Zhu, N. Sullivan, L. Zhu, L. Bian, D. Jennings, R. O'Hayre, Highly efficient reversible protonic ceramic electrochemical cells for power generation and fuel production, Nat. Energy. 4 (2019) 230–240. https://doi.org/10.1038/s41560-019-0333-2.

[4] J. Dailly, M. Ancelin, M. Marrony, Long term testing of BCZY-based protonic ceramic fuel cell PCFC: Micro-generation profile and reversible production of hydrogen and electricity, Solid State Ionics. 306 (2017) 69–75. https://doi.org/10.1016/j.ssi.2017.03.002.

[5] M. Marrony, J. Dailly, Advanced Proton Conducting Ceramic Cell as Energy Storage Device, ECS Meet. Abstr. MA2017-03 (2017) 305–305. https://doi.org/10.1149/ma2017-03/1/305.

[6] S. Choi, T.C. Davenport, S.M. Haile, Protonic ceramic electrochemical cells for hydrogen production and electricity generation: Exceptional reversibility, stability, and demonstrated faradaic efficiency, Energy Environ. Sci. 12 (2019) 206–215. https://doi.org/10.1039/c8ee02865f.

[7] H. Ding, W. Wu, C. Jiang, Y. Ding, W. Bian, B. Hu, P. Singh, C.J. Orme, L. Wang, Y. Zhang, D. Ding, Self-sustainable protonic ceramic electrochemical cells using a triple conducting electrode for hydrogen and power production, Nat. Commun. 11 (2020). https://doi.org/10.1038/s41467-020-15677-z.

[8] S. Yoo, A. Jun, Y.-W. Ju, D. Odkhuu, J. Hyodo, H.Y. Jeong, N. Park, J. Shin, T. Ishihara, G. Kim, Development of double-perovskite compounds as cathode materials for low-temperature solid oxide fuel cells., Angew. Chem. Int. Ed. Engl. 53 (2014) 13064–13067. https://doi.org/10.1002/anie.201407006.

[9] D. Jeong, A. Jun, Y.W. Ju, J. Hyodo, J. Shin, T. Ishihara, T.H. Lim, G. Kim, Structural, Electrical, and Electrochemical Characteristics of $LnBa_{0.5}Sr_{0.5}Co_{1.5}Fe_{0.5}O_{5+\delta}$ (Ln=Pr, Sm, Gd) as Cathode Materials in Intermediate-Temperature Solid Oxide Fuel Cells, Energy Technol. 5 (2017) 1337–1343. https://doi.org/10.1002/ente.201600618.

[10] G.C. Mather, D. Muñoz-Gil, J. Zamudio-García, J.M. Porras-Vázquez, D. Marrero-López, D. Pérez-Coll, Perspectives on cathodes for protonic ceramic fuel cells, Appl. Sci. 11 (2021). https://doi.org/10.3390/app11125363.

[11] Q. Yang, D. Tian, R. Liu, H. Wu, Y. Chen, Y. Ding, X. Lu, B. Lin, Exploiting rare-earth-abundant layered perovskite cathodes of $LnBa_{0.5}Sr_{0.5}Co_{1.5}Fe_{0.5}O_{5+\delta}$ (Ln=La and Nd) for SOFCs, Int. J. Hydrogen Energy. 46 (2021) 5630–5641. https://doi.org/10.1016/j.ijhydene.2020.11.031.

[12] B.S. Teketel, B.A. Beshiwork, X. Luo, D. Tian, S. Zhu, H.G. Desta, Q. Yang, Y. Chen, B. Lin, A-site doping enabled higher-oxygen-vacancy cobalt-free layered perovskite cathode for higher-performing protonic ceramic fuel cells, Ceram. Int. 48 (2022) 37232–37241. https://doi.org/10.1016/j.ceramint.2022.08.301.

[13] B. Lin, Z. Shangquan, L. Zhang, L. Bi, H. Ding, X. Liu, J. Gao, G. Meng, Prontonic ceramic membrane fuel cells with layered $GdBaCo_2O_{5+x}$ cathode prepared by gel-casting and suspension spray, J. Power Sources. 177 (2008) 330–333. https://doi.org/10.1016/j.jpowsour.2007.11.109.

[14] B. Lin, Y. Dong, R. Yan, S. Zhang, M. Hu, Y. Zhou, G. Meng, In situ screen-printed $BaZr_{0.1}Ce_{0.7}Y_{0.2}O_{3-\delta}$ electrolyte-based protonic ceramic membrane fuel cells with layered $SmBaCo_2O_{5+x}$ cathode, J. Power Sources. 186 (2009) 446–449. https://doi.org/10.1016/j.jpowsour.2008.09.120.

[15] H. Ding, X. Xue, X. Liu, G. Meng, A novel layered perovskite cathode for proton conducting solid oxide fuel cells, J. Power Sources. 195 (2010) 775–778. https://doi.org/10.1016/j.jpowsour.2009.08.022.

[16] J. Kim, S. Sengodan, G. Kwon, D. Ding, J. Shin, M. Liu, G. Kim, Triple-Conducting Layered Perovskites as Cathode Materials for Proton-Conducting Solid Oxide Fuel Cells, ChemSusChem. 7 (2014) 2811–2815. https://doi.org/10.1002/cssc.201402351.
[17] S. Choi, C.J. Kucharczyk, Y. Liang, X. Zhang, I. Takeuchi, H. Il Ji, S.M. Haile, Exceptional power density and stability at intermediate temperatures in protonic ceramic fuel cells, Nat. Energy. 3 (2018) 202–210. https://doi.org/10.1038/s41560-017-0085-9.
[18] A. Jun, S. Yoo, Y.W. Ju, J. Hyodo, S. Choi, H.Y. Jeong, J. Shin, T. Ishihara, T.H. Lim, G. Kim, Correlation between fast oxygen kinetics and enhanced performance in Fe doped layered perovskite cathodes for solid oxide fuel cells, J. Mater. Chem. A. 3 (2015) 15082–15090. https://doi.org/10.1039/c5ta02158h.
[19] G. Taillades, P. Pers, V. Mao, M. Taillades, High performance anode-supported proton ceramic fuel cell elaborated by wet powder spraying, Int. J. Hydrogen Energy. 41 (2016) 12330–12336. https://doi.org/10.1016/j.ijhydene.2016.05.094.
[20] K. Katahira, Y. Kohchi, T. Shimura, H. Iwahara, Protonic Conduction in Zr-Substituted BaCeO3, Solid State Ionics. 138 (2000) 91–98. https://doi.org/10.1016/S0167-2738(00)00777-3.
[21] S.P. Jiang, Activation, microstructure, and polarization of solid oxide fuel cell cathodes, J. Solid State Electrochem. 11 (2006) 93–102. https://doi.org/10.1007/s10008-005-0076-9.
[22] L.Q. Le, C. Meisel, C.H. Hernandez, J. Huang, Y. Kim, R. O'Hayre, N.P. Sullivan, Performance degradation in proton-conducting ceramic fuel cell and electrolyzer stacks, J. Power Sources. 537 (2022) 231356. https://doi.org/10.1016/j.jpowsour.2022.231356.
[23] J. Nielsen, M. Mogensen, SOFC LSM:YSZ cathode degradation induced by moisture: An impedance spectroscopy study, Solid State Ionics. 189 (2011) 74–81. https://doi.org/10.1016/j.ssi.2011.02.019.
[24] A. Nechache, A. Mansuy, M. Petitjean, J. Mougin, F. Mauvy, B.A. Boukamp, M. Cassir, A. Ringuedé, Diagnosis of a cathode-supported solid oxide electrolysis cell by electrochemical impedance spectroscopy, Electrochim. Acta. 210 (2016) 596–605. https://doi.org/10.1016/j.electacta.2016.05.014.
[25] P. Pers, V. Mao, M. Taillades, G. Taillades, Electrochemical behavior and performances of Ni-$BaZr_{0.1}Ce_{0.7}Y_{0.1}Yb_{0.1}O_{3-\delta}$ cermet anodes for protonic ceramic fuel cell, Int. J. Hydrogen Energy. 43 (2018) 2402–2409. https://doi.org/10.1016/j.ijhydene.2017.12.024.
[26] A. Subardi, M.H. Cheng, Y.P. Fu, Chemical bulk diffusion and electrochemical properties of $SmBa_{0.6}Sr_{0.4}Co_2O_{5+\delta}$ cathode for intermediate solid oxide fuel cells, Int. J. Hydrogen Energy. 39 (2014) 20783–20790. https://doi.org/10.1016/j.ijhydene.2014.06.134.
[27] A. Hammouche, E. Siebert, A. Hammou, M. Kleitz, A. Caneiro, Electrocatalytic Properties and Nonstoichiometry of the High Temperature Air Electrode $La_{1-x}Sr_x MnO_3$, J. Electrochem. Soc. 138 (1991) 1212. https://doi.org/10.1149/1.2085761.
[28] M.Z. Khan, A. Iltaf, H.A. Ishfaq, F.N. Khan, W.H. Tanveer, R.H. Song, M.T. Mehran, M. Saleem, A. Hussain, Z. Masaud, Flat-tubular solid oxide fuel cells and stacks: a review, J. Asian Ceram. Soc. 9 (2021) 745–770. https://doi.org/10.1080/21870764.2021.1920135.
[29] W. Bujalski, J. Paragreen, G. Reade, S. Pyke, K. Kendall, Cycling studies of solid oxide fuel cells, J. Power Sources. 157 (2006) 745–749. https://doi.org/10.1016/j.jpowsour.2006.01.060.
[30] M. Hanasaki, C. Uryu, T. Daio, T. Kawabata, Y. Tachikawa, S.M. Lyth, Y. Shiratori, S. Taniguchi, K. Sasaki, SOFC Durability against Standby and Shutdown Cycling, J. Electrochem. Soc. 161 (2014) F850–F860. https://doi.org/10.1149/2.0421409jes.
[31] D. Clematis, A. Barbucci, S. Presto, M. Viviani, M.P. Carpanese, Electrocatalytic activity of perovskite-based cathodes for solid oxide fuel cells, Int. J. Hydrogen Energy. 44 (2019) 6212–6222. https://doi.org/https://doi.org/10.1016/j.ijhydene.2019.01.128.
[32] A. Giuliano, M.P. Carpanese, D. Clematis, M. Boaro, A. Pappacena, F. Deganello, L.F. Liotta, A. Barbucci, Infiltration, Overpotential and Ageing Effects on Cathodes for Solid Oxide Fuel Cells: $La_{0.6}Sr_{0.4}Co_{0.2}Fe_{0.8}O_{3-\delta}$ versus $Ba_{0.5}Sr_{0.5}Co_{0.8}Fe_{0.2}O_{3-\delta}$, J. Electrochem. Soc. 164 (2017) F3114. https://doi.org/10.1149/2.0161710jes.

[33] M. Marrony, J. Dailly, Advanced Proton Conducting Ceramic Cell as Energy Storage Device, J. Electrochem. Soc. 164 (2017) F988–F994. https://doi.org/10.1149/2.1541709jes.
[34] B. Wei, M. Schroeder, M. Martin, Surface Cation Segregation and Chromium Deposition on the Double-Perovskite Oxide $PrBaCo_2O_{5+\delta}$, ACS Appl. Mater. Interfaces. 10 (2018) 8621–8629. https://doi.org/10.1021/acsami.7b17881.
[35] J.P. Kim, E. Magnone, M.J. Seo, J.H. Park, Development of novel chromium-tolerate barium–chromium oxide coated BSCF membrane for oxygen separation, Mater. Lett. 93 (2013) 383–385. https://doi.org/https://doi.org/10.1016/j.matlet.2012.11.008.
[36] M.A. Hassan, O. Bin Mamat, M. Mehdi, Review: Influence of alloy addition and spinel coatings on Cr-based metallic interconnects of solid oxide fuel cells, Int. J. Hydrogen Energy. 45 (2020) 25191–25209. https://doi.org/10.1016/j.ijhydene.2020.06.234.